PHYSICAL REVIEW B **98**, 134405 (2018)

Multiferroic properties of $R\mathrm{Fe}_{0.5}\mathrm{Co}_{0.5}\mathrm{O}_3$ with R = Tm, Er, Ho, Dy, and Tb

J. Lohr,[1] F. Pomiro,[2,*] V. Pomjakushin,[3] J. A. Alonso,[4] R. E. Carbonio,[2] and R. D. Sánchez[1,†]
[1]*Centro Atómico Bariloche, Comisión Nacional de Energía Atómica and Instituto Balseiro, Universidad Nacional de Cuyo, (8400) San Carlos de Bariloche (RN), Argentina*
[2]*Instituto de Investigaciones en Fisicoquímica de Córdoba (Consejo Nacional de Investigaciones Científicas y Técnicas [CONICET]–Universidad Nacional de Córdoba), Departamento de Fisicoquímica, Facultad de Ciencias Químicas, Universidad Nacional de Córdoba, Haya de la Torre Esq. Medina Allende, Ciudad Universitaria, X5000HUA Córdoba, Argentina*
[3]*Laboratory for Neutron Scattering and Imaging (LNS), Paul Scherrer Institute, Villigen CH-5232, Switzerland*
[4]*Instituto de Ciencia de Materiales de Madrid, CSIC, Cantoblanco, 28049 Madrid, Spain*

(Received 10 April 2018; revised manuscript received 3 August 2018; published 3 October 2018)

We present a detailed study of the thermal dependence of the neutron powder diffraction (NPD) of $R\mathrm{Fe}_{0.5}\mathrm{Co}_{0.5}\mathrm{O}_3$ perovskites (R = Tm, Er, Ho, Dy, and Tb) combined with a complete characterization of their magnetic, electric transport and ferroelectric properties. All samples are described with an orthorhombic (*Pbnm*) crystallographic structure. The inverse of magnetic susceptibility at high temperature shows an effective magnetic moment with contributions of high-spin Co^{3+}, Fe^{3+}, and the corresponding rare-earth cations (R^{3+}) moments. Negative Curie-Weiss temperatures indicate antiferromagnetic (AFM) correlations between the magnetic ions. At low temperature, the reduced magnetic saturation values are associated with crystal-field effects on R^{3+} ions. Below 300 K, magnetic reflections in NPD data show that the spin configuration in the ordered state is AFM type-G with a weak ferromagnetic component along the c axis (Γ_4) for transition metal ions. Spin reorientation (SR) transitions are observed, changing the irreducible representation from Γ_4 (G_x) to $\Gamma_2(G_z)$ at low temperatures, except for the Ho compound where it changes from Γ_4 (G_x) to $\Gamma_1(G_y)$. Magnetization data under field cooling (FC) and zero field cooling (ZFC) protocols show reversal magnetization for R = Er and Tb. A significant change of the slope of the M vs T curves is associated with the onset of magnetic order ($T_{N1} \sim 250\,\mathrm{K}$) of Fe/Co sublattice. The electric conductivity at room temperature shows that Tm value is ten times less than the other rare earths. The temperature dependence of the electrical conductivity can be described with a variable range hopping model ($\ln\sigma \sim T^{-1/4}$). Also, in the Tm case, the complex electrical permittivity shows a different behavior in comparison with the other members of the series. Finally, the Tm sample can be polarized when the specimen is cooled under different values of electrical field (E). Pyroelectric current can be detected while the sample is warming and depolarized, showing the ferroelectric critical temperature (T_C) at T_{N1}. A low electric polarization of 400 $\mu\mathrm{C/m}^2$ was measured for $\mathrm{TmFe}_{0.5}\mathrm{Co}_{0.5}\mathrm{O}_3$.

DOI: 10.1103/PhysRevB.98.134405

I. INTRODUCTION

Nowadays, multiferroic materials have attracted a lot of attention owing to their magnetoelectric (ME) effect. In a multiferroic material, magnetic and ferroelectric orderings coexist. However, the coexistence of these two kinds of order in the same material does not necessarily imply that they are strongly coupled with each other, i.e., ME coupling. Materials with ME effects have become of particular interest for understanding the fundamental physical links between spin, charge and lattice degrees of freedom that give rise to ME coupling. Then, exists the promising possibility of using these coupled order parameters in novel device applications by controlling the magnetization (polarization) with an electric field (magnetic field) [1–7].

Due to the enormous flexibility in composition and the wide extent of properties that can be achieved with the perovskite structure, these materials have been considered as a toolbox for materials chemists and physicists. Among the variety of unusual physical properties that perovskites exhibit, one of the most important is the cross coupling of magnetism and ferroelectricity (FE) observed in some members of the family.

Most of the rare-earth orthoferrites $R\mathrm{FeO}_3$ ($R = \mathrm{Pr} - \mathrm{Lu}$) have a similar orthorhombic distorted perovskite structure with *Pbnm* space group. The exchange interaction between iron ions ($J_{\text{Fe-Fe}}$) determine the temperature T_{N1} ranging from 630 to 650 K. The Fe^{3+} magnetic moments undergo a magnetic phase transition into a slightly canted antiferromagnetic structure with a very small ferromagnetic component due to the Dzyaloshinskii-Moriya interaction [8,9]. Generally, the magnetic order for the rare-earth sublattices occurs at a temperature T_{N2} below ~8 K ($J_{\text{R-R}} \ll J_{\text{Fe-Fe}}$), and above this temperature these magnetic moments are paramagnetic. However, the rare-earth ions experience the molecular field of the transition metal sublattices and due to the interaction between

---

[*] Present Address: Instituto de Física del Litoral (Universidad Nacional del Litoral-CONICET), Güemes 3450, S3000GLN Santa Fe, Argentina.

[†] Corresponding author: rodo@cab.cnea.gov.ar

both sublattice ($J_{\text{Fe-R}}$), the R magnetic moments are partially magnetized [8]. Consequently, at temperatures lower than T_{N1} both $J_{\text{Fe-Fe}}$ and $J_{\text{Fe-R}}$ play an important role in the magnetic behavior of these compounds and $J_{\text{Fe-R}}$ could produce the vastly studied phenomena called spin reorientation (SR) and magnetization reversal (MR).

As stated above, ferroelectricity has been observed in orthoferrites, as is the case of $LuFeO_3$, however, presents a weak polarization [10]. Also, pyroelectric current measurements have shown a ferroelectric behavior on $SmFeO_3$ single crystals and first-principles calculations indicate that the canted antiferromagnetic order is responsible for the ferroelectricity [11]. In addition, ferroelectric hysteresis curves and polarization (P) versus electric field (E) curves were reported for $YFeO_3$ and $LaFeO_3$ [12,13].

On the other hand, rare-earth cobaltites RCoO$_3$ with a perovskite-type structure have been extensively studied for a long time because of their interesting electronic and magnetic properties [14,15]. Except $LaCoO_3$ that crystallizes in the rhombohedral *R-3c* space group, the rest of the members of the family ($R = \text{Pr} - \text{Lu}$) have orthorhombic structures and belong to the *Pbnm* space group [16]. Interest in these compounds has been mainly associated with electric and magnetic transitions, which are related to the ability of Co^{3+} to present various spin states, i.e., low-spin (LS), high-spin (HS), and intermediate-spin (IS). This happens because the crystal-field splitting Δ_{CF} between the t_{2g} and e_g states is only slightly larger than the Hund coupling energy and the system can be thermally excited to either HS or IS configuration. In RCoO$_3$, the ground state of the localized Co^{3+} ions is the nonmagnetic state ($S = 0$) that corresponds to the LS ($t_{2g}{}^6e_g{}^0$) configuration. As mentioned above, the transition to a paramagnetic state is associated with a thermal excitation to the IS ($t_{2g}{}^5e_g{}^1$, S = 1) or HS ($t_{2g}{}^4e_g{}^2$, S = 2) Co^{3+} states [17].

It is known that mixtures of cations in a single material can help to achieve new properties, but also it is true that it adds further complexity to the system. Chemical substitution at the Fe site in RFeO$_3$ brings about interesting multiferroic effects. For example, in $YFe_{1-x}M_xO_3$ (M = Mn and Cr), magnetoelectric and magnetodielectric effects were reported [18,19]. Spin-reorientation effects, reversal magnetization, negative thermal expansion (NTE), and magnetic sublattice effects were also observed in doped-orthoferrites with Cr and Mn [20–22].

In this paper, we report combined neutron powder diffraction, magnetization, electrical conductivity, and dielectric and pyroelectric current measurements on RFe$_{0.5}$Co$_{0.5}$O$_3$ (R = Tm, Er, Ho, Dy and Tb) compounds. The substitution of 50% of Fe^{3+} cation in RFeO$_3$ by the closest isovalent and nonmagnetic (at least at very low temperature) Co^{3+}, was chosen in order to obtain magnetic transitions and electric polarization near room temperature [$J_{\text{Fe-Fe}} > J_{\text{(Fe/Co)-(Fe/Co)}}$]. In the other hand, changing R in the RFe$_{0.5}$Co$_{0.5}$O$_3$ series allow us to make a systematic study, keeping practically constant $J_{\text{(Fe/Co)-(Fe/Co)}}$ and effectively changing the $J_{\text{(Fe/Co)-R}}$ magnetic exchange interaction for each compound. We show that all the compounds of the series show a rich variety of magnetic phases and properties such as SR, magnetization reversal, and negative thermal expansion, and only the Tm sample shows electric remanent polarization. We summarized all these results in a magnetic and electrical phase diagram.

II. EXPERIMENTAL PROCEDURE

The cyano-metal complexes, $R[Fe_{0.5}Co_{0.5}(CN)_6] \cdot 4H_2O$ (R = Tm, Er, Ho, Dy, Tb) as precursors of perovskite-type oxides, RFe$_{0.5}$Co$_{0.5}$O$_3$, were prepared according to the reported method [23,24], by slowly dropping a solution of $R(NO_3)_3$ on a solution containing stoichiometric amounts of $K_3[Fe(CN)_6]$ and $K_3[Co(CN)_6]$ under continuous stirring at 333 K for 2 h. The resulting precipitates were separated by filtration, washed with water and ethanol and finally stored in the dark in a dry box with silica gel. The precursor powders were heat-treated in a furnace at 1223 K during 6 h to yield perovskite-type oxides RFe$_{0.5}$Co$_{0.5}$O$_3$.

The samples were characterized by x-ray powder diffraction method (XRPD) using a PANalytical X'Pert PRO diffractometer in a Bragg-Brentano configuration and Cu-K_α radiation. XRPD data were collected in the angular 2θ range $5^\circ - 120^\circ$ in steps of 0.02° and with a collection time of 10 s/step. Neutron powder diffraction (NPD) experiments were carried out in the HRPT instrument at the SINQ facility in the Paul Scherrer Institute (PSI), Villigen, Switzerland. In this instrument, the patterns were collected at various temperatures, between room temperature and 2 K, for each sample with a $\lambda = 1.494$ Å in the 2θ range from 8.0° to 160°, with increments of 0.05°. The refinement of crystal structures from XRPD and NPD data were performed using Rietveld method [25] with the FULLPROF program [26]. A Thompson-Cox-Hastings pseudo Voigt function was chosen to generate the line shape of diffraction peaks. The following parameters were refined: scale factor, background coefficients, zero shift, peak shape parameters, atomic positional and thermal factors, unit-cell parameters, and occupancies of the rare-earth and transition metal cations.

The magnetic measurements were performed with a commercial Quantum Design MPMS-5S superconducting quantum interference device (SQUID) on powder samples, in the 5–320 K temperature (T) range and magnetic field (H) up to 50 kOe. Magnetization versus temperature measurements were collected at $H = 5000$ and 100 Oe. The curves collected at $H = 100$ Oe were measured following the zero-field cooling (ZFC) and field cooling (FC) protocol. From room temperature to 1000 K the M versus T curves were acquired in a home-made Faraday balance at $H = 5000$ Oe.

All the electrical properties have been measured on specimens with disk shape. Electrodes with a diameter of around 5 mm were placed on the disk faces, with a separation between each other of approximately 0.5 mm (thickness of the disk). Electrical conductivity (σ) as a function of temperature was measured with the two-probe technique from 77 K to room temperature applying 200 V and measuring current trough samples in a home-made device. It includes a Keithley 6517A electrometer and a Lake Shore 330 temperature controller. The electrical contacts were made by applying silver paint. In the same home-made device, using an Andeen-Hagerling 2500A ultraprecision capacitance bridge, we measured the capacitance and the loss with 1 kHz excitation, calculating the complex electrical permittivity (ϵ' and ϵ'', respectively). The

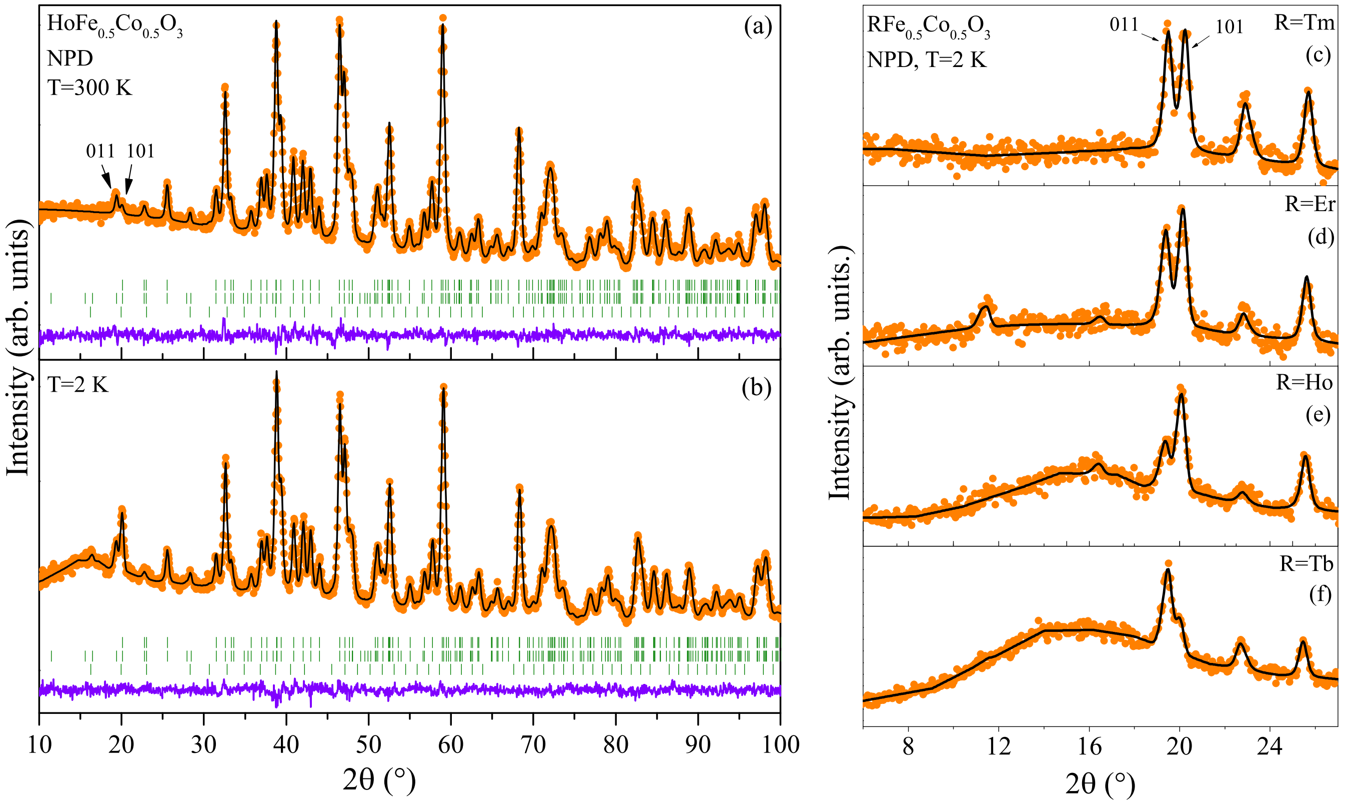

FIG. 1. (Left) Observed (orange circles) and calculated (solid black line) NPD patterns at (a) 300 and (b) 2 K with $\lambda = 1.49214(2)$ Å for $\text{HoFe}_{0.5}\text{Co}_{0.5}\text{O}_3$. The three series of tick marks correspond to the nuclear Bragg reflections of the main phase and impurity (upper and middle) and the magnetic peaks (lower). The difference pattern is plotted at the bottom (violet solid line). (Right) Detail view from 6° to 27°of the NPD patterns measured at 2 K for $R\text{Fe}_{0.5}\text{Co}_{0.5}\text{O}_3$ with $R =$ (c) Tm, (d) Er, (e) Ho, and (f) Tb. The Dy pattern it is not included. Magnetic Bragg reflections (101) and (011) are labelled only for the Tm case.

samples were tested with a parallel plate capacitor and the electrical contacts were made with silver paint. Pyroelectric current was measured using the same home-made equipment. Samples were cooled with an applied field ±3.5 kV/cm, and the pyroelectric current was detected with the electrometer while the temperature increases at 2 K/min. The electrical polarization (P) as a function of temperature was obtained by integrating the current.

III. RESULTS

A. Crystallographic characterization, magnetic order and determination of the magnetic structure

NPD data for $R\text{Fe}_{0.5}\text{Co}_{0.5}\text{O}_3$ ($R =$ Tm, Er, Ho, Dy, and Tb) compounds at 300 K were successfully refined using the *Pbnm* (No. 62) space group ($Z = 4$) with $a_p\sqrt{2}$, $a_p\sqrt{2}$, $2a_p$ cell parameters (a_p referring to the ideal cubic perovskite). In this structure, the rare-earth cations (R^{3+}) occupy the 4c (x, y, 1/4) sites, $\text{Fe}^{3+}/\text{Co}^{3+}$ cations are randomly distributed at the 4b (0, 1/2, 0) sites and are octahedrally coordinated by O^{2-} anions, which occupy two different Wyckoff positions [4c (x, y, 1/4) and 8d (x, y, z)]. To obtain the chemical formula of these $R\text{Fe}_{0.5}\text{Co}_{0.5}\text{O}_3$ compounds, the Fe/Co occupancy in the 4b site was refined from the NPD data since this could not be performed based on XRPD data because the x-ray scattering factors for Fe^{3+} and Co^{3+} ions are very similar. These occupancies can be determined and in a very precise way by NPD due to the high difference in the scattering lengths for Fe and Co (9.45 and 2.49 fm, respectively). The good agreement between the observed and calculated patterns of $\text{HoFe}_{0.5}\text{Co}_{0.5}\text{O}_3$ at 300 K is shown in Fig. 1(a). In all the samples a small amount of $R_2\text{O}_3$ was detected (less than 2%). Table I summarizes the unit cell, atomic positions, occupancies, atomic displacement parameters and reliability factors obtained from NPD data for $R\text{Fe}_{0.5}\text{Co}_{0.5}\text{O}_3$ perovskites at 300 K. Additionally, Table I shows the calculated chemical formulas obtained for the samples. The transition metal compositions are in excellent agreement with the nominal ones. These compositions also suggest that some vacancies of R and O ions are systematically present in the samples but no Fe and Co impurity compounds have been detected neither by XRPD nor by NPD. This may indicate that these impurities are below the detection limit of the technique or that the crystallinity is not good enough to be detected.

As shown in Fig. 1(a), some reflections in the room temperature NPD pattern are not indexed with the *Pbnm* space group. For instance the (011) reflection forbidden in *Pbnm* is observed even at 300 K with a very small intensity. These peaks are magnetic reflections.

The thermal evolution of lattice parameters for $R\text{Fe}_{0.5}\text{Co}_{0.5}\text{O}_3$ ($R =$ Tm, Ho, and Tb) was examined by cooling from 300 to 2 K. The results are shown in Fig. SM1 in Ref. [27]. In the three cases the expected thermal expansion (TE) of the b and c unit cell parameters when temperature

TABLE I. Unit-cell parameters, atomic positions, occupancies, displacement factors, reliability factors, and refined composition obtained from NPD at 300 K for $R\mathrm{Fe}_{0.5}\mathrm{Co}_{0.5}\mathrm{O}_3$.

R^{3+}	Tm	Er	Ho	Dy	Tb
T (K)	300	300	300	300	300
a (Å)	5.1755(3)	5.1922(5)	5.2111(5)	5.2334(3)	5.2630(4)
b (Å)	5.4907(2)	5.4500(4)	5.5025(2)	5.4986(4)	5.4965(3)
c (Å)	7.4399(2)	7.4609(3)	7.4792(4)	7.4956(4)	7.5226(5)
V (Å^3)	211.42(4)	213.05(6)	214.46(6)	215.70(5)	217.61(7)
R 4c (x, y, $1/4$)					
x	0.5185(5)	0.5170(5)	0.5168(4)	0.5152(3)	0.5141(3)
y	0.5710(3)	0.5693(3)	0.5681(3)	0.5656(2)	0.5630(2)
B(Å^2)	0.76(3)	0.91(3)	0.80(4)	0.80(3)	0.59(4)
Occup. (%)	98.2	99.2	98.8	98.8	98.8
(Fe, Co) 4b (0, ½, 0)					
B(Å^2)	0.53(4)	0.65(4)	0.58(3)	0.54(3)	0.49(4)
Occup. (%)	49.6/50.4	49.6/50.4	50.0/50.0	48.8/51.2	50.0/50.0
O1 4c (x, y, $1/4$)					
x	0.3939(5)	0.3970(5)	0.3980(5)	0.4036(8)	0.40454(4)
y	−0.0360(5)	−0.0353(5)	−0.0343(4)	−0.0325(7)	−0.0285(3)
B(Å^2)	0.87(4)	0.87(4)	0.95(5)	0.87(5)	0.72(3)
Occup. (%)	99.0	99.2	98.5	99.2	98.0
O2 8d (x, y, z)					
x	0.6915(3)	0.6913(3)	0.6938(3)	0.6923(5)	0.6970(2)
y	0.3040(4)	0.3040(4)	0.3030(4)	0.3038(6)	0.3005(2)
z	0.0553(2)	0.0537(2)	0.0528(2)	0.0510(6)	0.0491(2)
B(Å^2)	0.90(3)	1.04(3)	0.97(4)	1.06(4)	0.82(3)
Occup. (%)	100	100	100	100	100
Reliability factors					
χ^2	2.10	1.38	1.27	1.65	1.28
R_p(%)	3.52	3.17	2.95	12.10	2.76
R_{wp}(%)	5.10	4.04	3.77	3.45	3.51
R_{exp}(%)	3.52	3.44	3.34	2.68	3.10
R_{Bragg}(%)	1.67	1.58	1.36	1.84	1.31
R_{Mag}(%)	3.26	3.39	9.20	9.40	9.30
Refined composition	$\mathrm{Tm}_{0.982}\mathrm{Fe}_{0.495}\mathrm{Co}_{0.504}\mathrm{O}_{2.990}$	$\mathrm{Er}_{0.992}\mathrm{Fe}_{0.496}\mathrm{Co}_{0.503}\mathrm{O}_{2.991}$	$\mathrm{Ho}_{0.989}\mathrm{Fe}_{0.499}\mathrm{Co}_{0.501}\mathrm{O}_{2.985}$	$\mathrm{Dy}_{0.989}\mathrm{Fe}_{0.488}\mathrm{Co}_{0.512}\mathrm{O}_{2.991}$	$\mathrm{Tb}_{0.989}\mathrm{Fe}_{0.499}\mathrm{Co}_{0.501}\mathrm{O}_{2.979}$

increases is observed. In contrast, a NTE phenomenon is evidenced at low temperature in the a unit cell parameter, that is more evident in the cases of $R = \mathrm{Tm}$ and Tb. These results will be discussed later together with the magnetic structure determination.

The magnetization (M) curves versus temperature (T) at 100 Oe, after ZFC-FC protocols for $R = \mathrm{Tm}$, Ho, and Tb are presented in Figs. 2(a), 2(b), and 2(c) and the corresponding to $R = \mathrm{Er}$ and Dy are displayed in Figs. 3(a) and 3(b), respectively. The shift between ZFC and FC curves occurs, approximately at 215, 250, 285, 280, and 285 K for $R = \mathrm{Tm}$, Er, Ho, Dy, and Tb respectively, which could be associated with the magnetic order temperature. However, we took as the characteristic temperature (T_{N1}) to indicate the onset of magnetic order, the temperature where a significant change in the slope of M is observed [249(8), 250(5), 249(5), 252(5), and 254(9) K for $R = \mathrm{Tm}$, Er, Ho, Dy, and Tb, respectively]. These changes are close to 250 K for all samples and it is marked in the figures. Considering the increase of magnetization values after the transition and the magnetic order of the analogous $R\mathrm{FeO}_3$ compounds, we associated these changes with a broad transition towards a weak ferromagnetic order (or canted antiferromagnetic) state. This range of temperatures in the onset of the magnetic order is expected due to the substitution of 50% of Fe^{3+} cations in $R\mathrm{FeO}_3$ (onset of magnetic order between 630–650 K from Tm to Tb) by Co^{3+}. A similar decrease of the magnetic order temperature when Fe^{3+} cations are replaced with the diamagnetic Al^{3+} cations has been observed in LaFeO_3 [28,29]. Also, studies in $\mathrm{LaFe}_{1-x}\mathrm{Co}_x\mathrm{O}_3$ have shown a decrease on the magnetic order temperature as x increases [30].

Below T_{N1}, all samples exhibit an increase in magnetization, leading to a maximum (in the ZFC curves) followed by an abrupt drop, except for the Tb sample, where M has

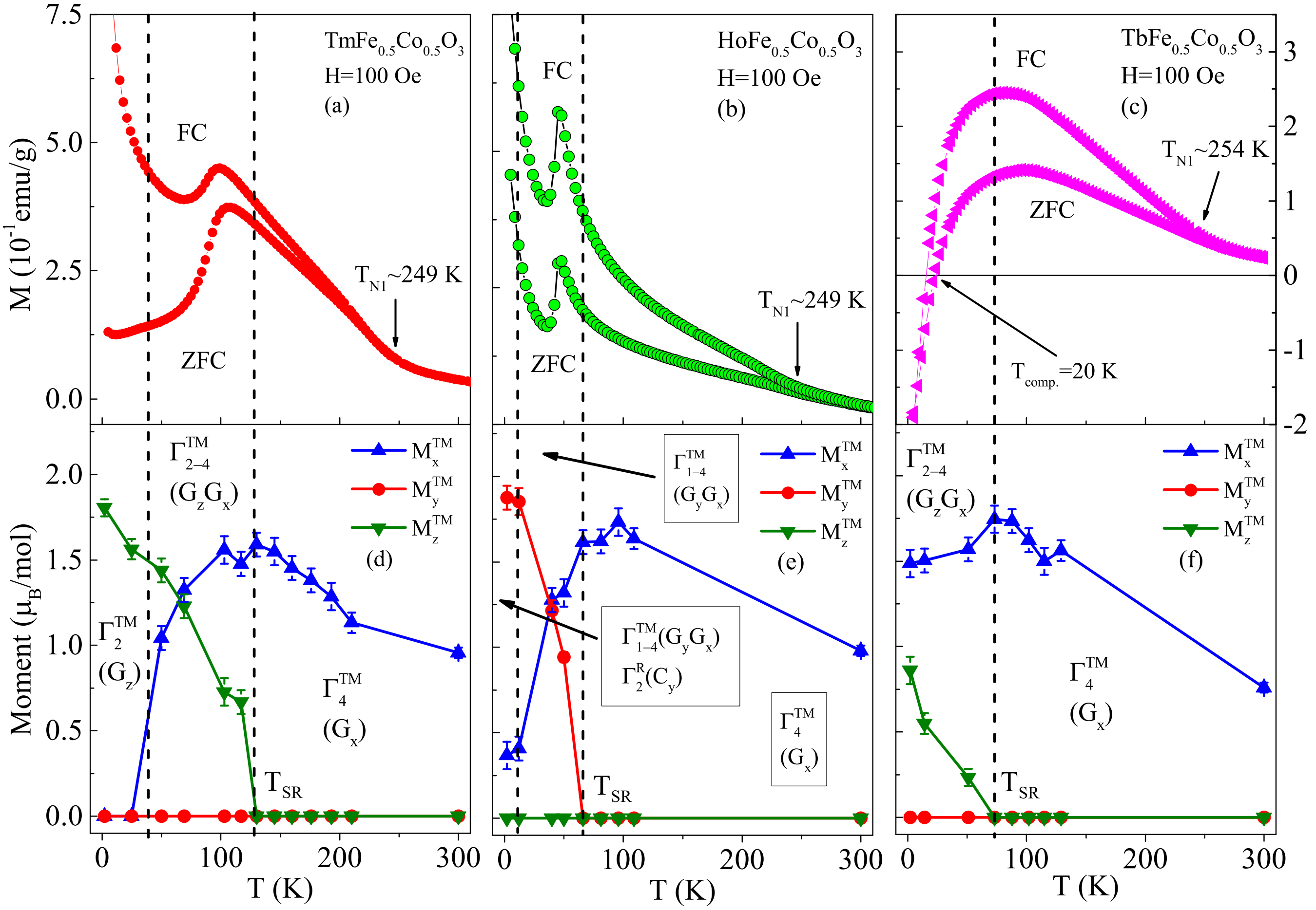

FIG. 2. (Top) [(a)–(c)] M vs T for ZFC and FC protocols, measured at $H = 100$ Oe for Tm, Ho, and Tb respectively. T_{N1} is a characteristic temperature associated with the magnetic order of the Fe/Co sublattice. Vertical lines indicate the SR temperature (T_{SR}). Magnetization reversal is observed in $R =$ Tb. (Bottom) [(d)–(f)] Temperature evolution of the three components of magnetic moment for the transition metal sublattice obtained from Rietveld refinement of NPD data at different temperatures. Irreducible representations of the magnetic phases are indicated.

a smooth change around the maximum. We associated these changes with SR of the Fe-Co sublattice. The temperatures of the maxima are Tm: (106 ± 5) K, Er: (81 ± 5) K, Ho: (45 ± 5) K, Dy: (90 ± 5) K, and Tb: (102 ± 30) K. The SR is caused by both anisotropic-symmetric exchange and antisymmetric Dzyaloshinskii-Moriya (DM) interactions between transition metal and rare-earth cations. The temperatures, at which this type of transition occurs, as well as the magnetic structures before and after SR, are all conditioned by the combination of cations and their magnetic interactions [31]. The presence of another transition metal cation in $R\mathrm{FeO}_3$ adds complexity to the behavior, because the magnitude of R^{3+}-Fe^{3+} coupling is modified and it is reflected in the SR temperatures. For example, it is known that the magnitude of R^{3+}-Cr^{3+} coupling is higher than R^{3+}-Fe^{3+} coupling, and this is why the SR take place at lower temperatures in $R\mathrm{FeO}_3$ than in $R\mathrm{CrO}_3$ considering the same R^{3+} cation [31,32]. In the case of $R\mathrm{Fe}_{0.5}\mathrm{Co}_{0.5}\mathrm{O}_3$, the SR temperatures are similar to the ones observed for $R\mathrm{FeO}_3$, because due to the diamagnetism of the Co^{3+} cations at low temperatures the R^{3+}-Fe^{3+} interaction is the unique responsible of the effect [8,33–38].

Initially, the magnetic structure determination of the $R\mathrm{Fe}_{0.5}\mathrm{Co}_{0.5}\mathrm{O}_3$ ($R =$ Tm, Er, Ho and Tb) samples was carried out from a set of NPD patterns measured at 2 K [see Fig. 1(b) for the Ho pattern and Figs. 1(c) to 1(f) for the others], but in some cases, NPD patterns at intermediate temperatures between 2 and 300 K were measured and analyzed to follow the evolution of the magnetic structures. The different magnetic groups associated with the propagation vector $k = (0, 0, 0)$ and compatible with the *Pbnm* space group were tabulated by Bertaut [39] and lead for the transition elements (B site of the perovskite) to four irreducible representations allowing a nonzero magnetic contribution. The B-site magnetic cations are present at *4b* sites at positions (1/2, 0, 0), (0, 1/2, 0), (1/2, 0, 1/2), and (0, 1/2, 1/2). Four base vectors representing the possible magnetic modes of coupling can be expressed according to Bertaut's notation: $F(++++)$, $G(+-+-)$, $C(+-+-)$, and $A(++--)$. The four irreducible representations known for orthoferrites [$\Gamma_1(A_xG_yC_z)$, $\Gamma_2(F_xC_yG_z)$, $\Gamma_3(C_xF_yA_z)$, and Γ_4 $(G_xA_yF_z)$] can be represented in terms of F, G, C, and A vector components along three crystallographic directions. On the other hand, the A-site (rare-earth site) magnetic cations are present at *4c* sites at positions $(x, y, 1/4)$, $(x + 1/2, -y + 1/2, 3/4)$, $(-x, -y, 3/4)$, and $(-x + 1/2, y + 1/2, 1/4)$. The irreducible representations are defined as $\Gamma_1(0\,0\,C_z)$,

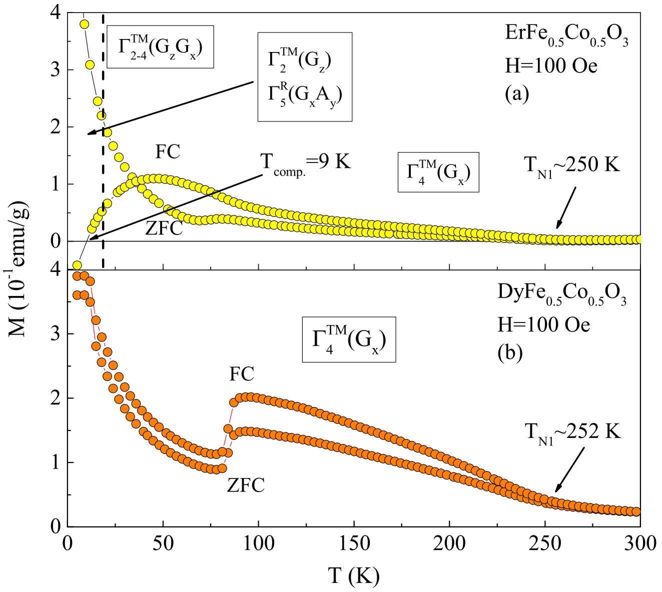

FIG. 3. [(a) and (b)] M vs T for ZFC and FC protocols, measured at $H = 100\,\mathrm{Oe}$ for Er and Dy, respectively. T_{N1} is a characteristic temperature associated with the magnetic order of the Fe/Co sublattice. The maximum of ZFC magnetization curves (Er: 80 K and Dy: 90 K) is associated to SR. Reversal magnetization is observed in $R = \mathrm{Er}$.

$\Gamma_2(F_xC_y0)$, $\Gamma_3(C_xF_y0)$, $\Gamma_4(0\,0\,F_z)$,$\Gamma_5(G_xA_y0)$, $\Gamma_6(0\,0\,A_z)$, $\Gamma_7(0\,0\,G_z)$, and $\Gamma_8(A_xG_y0)$.

In general, the NPD patterns collected at 300 K show some Bragg reflections with small intensities that were not correctly modeled with the crystal structure [see reflections 011 and 101 in Fig. 1(a) for the sample with Ho], which correspond to magnetic reflections. This indicates that long-range ordered regions exist above T_{N1}. This can be understood by the presence of small regions whose magnetism is dominated by Fe^{3+}-O-Fe^{3+} superexchange since the B cations are disordered in these perovskites, with sufficient coherence between neighboring regions to give rise to diffraction.

The synthesized perovskites share similarities in their magnetic structures. In all the cases, at the onset of magnetic order a G_x structure belonging to the Γ_4 representation is adopted. It is known that all rare-earth orthoferrites adopt this structure immediately below their order temperature [8]. It is important to notice that a ferromagnetic F component along the c axis and an A-type antiferromagnetic arrangement along the b axis are allowed by symmetry within the same irreducible representation, but the M_y and M_z components are either close to zero or below the sensitivity of NPD, and were consequently fixed to zero during the refinements.

As the temperature decreases, a slow SR transition toward $G_z(\Gamma_2)$ takes place in a finite temperature range for the sample with $R =$ Tm, Er, and Tb. For the case of Ho sample, the SR takes place toward a G_y ordering (Γ_1). In all cases, the spin structure during the SR has both G components (G_{xz} for Tm, Er and Tb and G_{xy} for Ho), and in the case of Ho and Tb, both G components are present even at 2 K (incomplete SR transition).

For the case of $TmFe_{0.5}Co_{0.5}O_3$, the G_x (Γ_4) to $G_z(\Gamma_2)$, SR takes place between 130 and 40 K. In this temperature range, the magnetic moments rotate from the a axis toward the c axis, remaining in the (a, c) plane. We take $T_{SR} \sim 130\,\mathrm{K}$ as SR temperature for this perovskite. The excellent agreement between the experimental and calculated NPD patterns shown in Fig. 1(c) (only the low angle region is shown in the figure) taken at 2 K was obtained considering only the long-range magnetic order of the transition metal sublattices and it was not necessary to include a magnetic structure for the rare-earth sublattice (see Table II). Figures 2(a) and 2(d) illustrate the agreement between macroscopic magnetic measurements and temperature dependence of the magnetic moments: the SR temperature range determined by NPD is in perfect agreement with the shape of the ZFC-FC magnetization curves.

In the case of the Er sample, we have only NPD patterns measured at 2, 60, and 300 K. The thermal evolution of the magnetic reflections is very similar to the case of the Tm sample. A SR transition takes place from Γ_4 (G_x) to $\Gamma_2(G_z)$. The main difference is that at 2 K it is necessary to include the Er^{3+} contribution to refine the magnetic structure. The best refinement was obtained with an AFM $\Gamma_5(G_xA_y0)^R$ irreducible representation for the rare-earth cations, where the magnetic moments develop a value of 0.63 and 0.77 μ_B/ per site in the x and y direction, respectively (see Table II). The excellent agreement between the experimental and calculated NPD patterns collected at 2 K can be observed in Fig. 1(d). In the ZFC/FC plot a maximum at 80 K [Fig. 3(a)] is detected. We take this temperature as close than the SR one ($T_{SR} \sim 80\,\mathrm{K}$). Below this temperature, both G_{xz} components are present. The rare-earth magnetic moments rotate and these align antiparallel with respect to the transition-metal lattice, given the negative magnetization (or magnetization reversal) due to the large R^{3+} magnetic moment. The temperature where the magnetization crosses zero is called compensation temperature ($T_{comp} \sim 9\,\mathrm{K}$).

$HoFe_{0.5}Co_{0.5}O_3$ NPD data at 2 K are shown in Fig. 1(b) and a zoom view of the low angle region is displayed in Fig. 1(e). One big difference with the two previously described compounds is that the (101) magnetic reflection is much more intense than the (011) one. In this case, on the contrary to the case of Tm and Er, there is an incomplete SR transition taking place from Γ_4 (G_x) to $\Gamma_1(G_y)$, starting at 56 K. From 56 to 2 K the magnetic moments of the transition metal ions rotate from the a axis toward the b axis, staying in the (a, b) plane, but never reaching completely the b axis [see Fig. 2(e)]. At approximately 10 K, it is necessary to include the Ho^{3+} contribution to refine the magnetic structure. The best refinement was obtained with an AFM $\Gamma_2(C_y)^R$ irreducible representation for the rare-earth cations, where the magnetic moments are along the y axis (crystallographic b axis) and develops a magnetic moment value of 0.7 μ_B/f.u. Even though the Ho^{3+} cations are magnetically ordered below 10 K, the Ho^{3+} ions develop no significant magnetic moment. If we compare the Ho^{3+} magnetic moment developed by $HoCoO_3$ (6.48 μ_B/f.u) and $HoFeO_3$ (8.65μ_B/f.u) below 3 and 6.1 K, respectively [36,40], we noted that in $HoFe_{0.5}Co_{0.5}O_3$, the Ho^{3+} order it is not fully developed. This is in agreement with the high values of background observed in the low angle region of Fig. 1(e), which indicate short-range magnetic order of the Ho^{3+} magnetic moments. The excellent agreement between the experimental and calculated NPD pat-

TABLE II. Magnetic moment components M_x, M_y, and M_z and magnetic moment module obtained from NPD at 2 and 300 K for $R\mathrm{Fe}_{0.5}\mathrm{Co}_{0.5}\mathrm{O}_3$. The magnetic moment values are expressed in μ_B/per site.

		Tm		Er		Ho		Dy		Tb	
		300 K	2 K	300 K	2 K	300 K	2 K	300 K	2 K	300 K	2 K
Irred. repres.		$\Gamma_4(G_xA_yF_z)$	$\Gamma_2(F_xC_yG_z)$	$\Gamma_4(G_xA_yF_z)$	$\Gamma_2(F_xC_yG_z)$	$\Gamma_4(G_xA_yF_z)$	$\Gamma_{4-1}(G_xG_y)$	$\Gamma_4(G_xA_yF_z)$		$\Gamma_4(G_xA_yF_z)$	$\Gamma_{4-2}(G_xA_yG_z)$
$\mathrm{Fe}^{3+}/\mathrm{Co}^{3+}$ sublattice	M_x	0.96(4)	0	0.98(4)	0	0.98(4)	0.37(4)	1.06(4)	—	0.76(4)	1.49(4)
	M_y	0	0	0	0	0	1.88(6)	0	—	0	0
	M_z	0	1.85(2)	0	1.93(3)	0	0	0	—	0	0.86
	$\lvert M\rvert$	0.96	1.85	0.98	1.93	0.98	1.92	1.06	—	0.76	1.72
Irred. repres.		—	—	—	$\Gamma_5(G_xA_y0)$	—	$\Gamma_2(F_xC_y0)$	—	—	—	—
R^{3+} sublattice	M_x	—	—	—	0.63(7)	—	0	—	—	—	—
	M_y	—	—	—	0.77(6)	—	0.70(4)	—	—	—	—
	M_z	—	—	—	0	—	0	—	—	—	—
	$\lvert M\rvert$	—	—	—	0.99	—	0.70	—	—	—	—

terns collected at 2 K can be observed in Figs. 1(b) and 1(e). Figures 2(b) and 2(e) illustrate the agreement between macroscopic magnetic measurements and temperature dependence of the magnetic moments: the SR temperature range determined by NPD is in perfect agreement with the shape of the ZFC-FC susceptibility curves.

The NPD data of $\mathrm{DyFe}_{0.5}\mathrm{Co}_{0.5}\mathrm{O}_3$ at 300 K are well described with a $\Gamma_4(G_x)$ representation and we don't have data at 2 K. The ZFC curve displayed in Fig. 3(b) show a maximum at 90 K, which may be associated with a SR transition.

The NPD data of $\mathrm{TbFe}_{0.5}\mathrm{Co}_{0.5}\mathrm{O}_3$ at 2 K are shown in Fig. 1(f) and the ZFC/FC curves are displayed in Fig. 2(c). In this case, the reflection (011) is more intense than (101) and an incomplete SR transition starts at 62 K, where the magnetic moments of the transition metal ions start to rotate from Γ_4 (G_x) to $\Gamma_2(G_z)$. A compensation temperature is observed at 20 K and it was not necessary to include the Tb^{3+} magnetic order for the refinements of the data, even at 2 K. In this case, also a short-range magnetic order of the Tb^{3+} magnetic moments is observed, shown by the high values of background observed in the low angle region [Fig. 1(f)]. In TbCoO_3 and TbFeO_3 the Tb^{3+} ions order at 3.6 and 8.5 K [37,39]. This indicates that the substitution of half of Fe^{3+} by Co^{3+} in TbFeO_3 destroys the Tb-magnetic order, showing that there is a strong influence of the transition metal magnetism on Tb-magnetic order. In Figs. 2(c) and 2(d), the good agreement between the M versus T curves and the thermal evolution of the magnetic moment components are shown. In Table II, we summarize the magnetic moment components (M_x, M_y, and M_z) obtained at 300 K and 2 K for the transition metal and rare-earth sites in $R\mathrm{Fe}_{0.5}\mathrm{Co}_{0.5}\mathrm{O}_3$.

By analyzing the NTE shown in Fig. SM1 (see Ref. [27]) and comparing it with the SR transition temperatures in the samples with $R =$ Tm, Ho and Tb, we can conclude that a clear magnetostrictive effect is observed in these samples, in a higher level in the samples with $R =$ Tm and Tb. A similar effect was observed by us on the related samples $R\mathrm{Fe}_{0.5}\mathrm{Cr}_{0.5}\mathrm{O}_3$ ($R =$ Yb and Tm) [20].

B. Paramagnetic properties

The magnetic susceptibility (χ) curves as a function of temperature at the magnetic field of $H = 5\,\mathrm{kOe}$ for $R\mathrm{Fe}_{0.5}\mathrm{Co}_{0.5}\mathrm{O}_3$ ($R =$ Tm, Er, Ho, Dy, Tb) are shown in Fig. 4. In the inset, the inverse of the magnetic susceptibility (χ^{-1}) versus temperature (T) is shown for all samples, after subtracting all the diamagnetic contributions. As was discussed in the previous section, below 250 K, the shift between ZFC and FC curves is due to the magnetic order in the samples. This order is also observed by NPD at low temperature. As we mentioned in the introduction, the paramagnetic phase in $R\mathrm{FeO}_3[T > T_N(R)]$ is reached, depending on the size of R^{3+}, above 620–650 K. In the perovskite system with disorder in the B cations like in $R\mathrm{Fe}_{0.5}\mathrm{Co}_{0.5}\mathrm{O}_3$, due to the presence of small regions whose magnetism is dominated by Fe^{3+}-O-Fe^{3+} superexchange, we expect that at temperatures above 700 K, the system should be well described with the Curie-Weiss law $[\chi = C/(T-\theta)]$, assuming that C and θ are temperature independent. Considering a linear χ^{-1} versus T behavior at $T >$ 700 K for all samples, the extrapolation of χ^{-1} to 0 gives

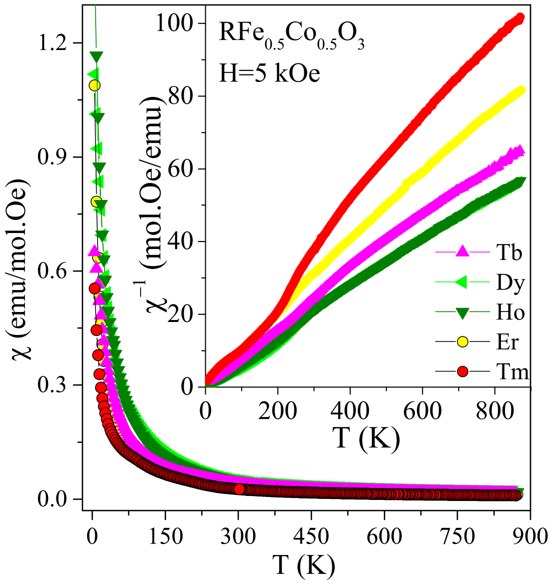

FIG. 4. Magnetic susceptibility (χ) as a function of temperature at $H = 5$ kOe for RFe$_{0.5}$Co$_{0.5}$O$_3$ (R = Tb, Dy, Ho, Er, and Tm). (Inset) Inverse magnetic susceptibility (χ^{-1}) vs temperature (T).

negative values of Weiss temperatures (θ), which indicates the presence of antiferromagnetic interactions between the magnetic ions. The slopes observed for the χ^{-1} versus T plots are principally affected by the effective magnetic moment of R^{3+} ion ($\mu_{\rm eff}$). The order of slopes from higher to lower are Tm, Er, Tb, Ho, and Dy (these two last curves are practically overlapped in the inset of Fig. 4). Using the slope $a = 1/C$ values, we estimated the experimental effective paramagnetic moment calculating as

$$\mu_{\rm eff}[\text{exp.}](T > 700\text{ K}) = \sqrt{\frac{3k}{N{\mu_{\rm B}}^2\, a}}, \quad (1)$$

where k is Boltzmann constant and $\mu_{\rm B}$ is the Bohr magneton. The $\mu_{\rm eff}$ [exp.] values obtained for Tm, Er, Tb, Ho, and Dy are 9.0(2), 10.4(2), 11.4(2), 11.8(2), and 12.0(2) $\mu_{\rm B}$, respectively.

Now, to compare with the theory, we can estimate the total calculated effective paramagnetic moment ($\mu_{\rm eff}$ [calc.]) as

$$\mu_{\rm eff}^2[\text{calc.}] = \mu_{\rm eff}^2[R^{3+}] + \tfrac{1}{2}\mu_{\rm eff}^2[\text{Fe}^{3+}(\text{HS})] + \tfrac{1}{2}\mu_{\rm eff}^2[\text{Co}^{3+}(\text{HS})], \quad (2)$$

where, $\mu_{\rm eff}[R^{3+}] = \text{g}\sqrt{J(J+1)} = 7.57$, 9.59, 9.72, 10.60, and 10.63 $\mu_{\rm B}$ for Tm, Er, Tb, Ho, and Dy; $\mu_{\rm eff}[\text{Fe}^{3+}(\text{HS})] = \text{g}\sqrt{S(S+1)} = 5.91\,\mu_{\rm B}$, and for $\mu_{\rm eff}[\text{Co}^{3+}(\text{HS})] = \text{g}\sqrt{S(S+1)} = 4.89\,\mu_{\rm B}$. Replacing the corresponding effective paramagnetic moments in Eq. [2] for Tm, Er, Tb, Ho and Dy, we obtained 9.09, 10.85, 11.03, 11.72, and 11.90 $\mu_{\rm B}$, respectively. These calculated values are in excellent agreement with the experimental effective paramagnetic moments.

Between 300 and 650 K, a deviation from the Curie-Weiss law is observed. As we mentioned above, it can be due to the magnetic correlation between the iron ions or to slight changes in the slope associated with spin state transitions of the Co^{3+} cations induced by temperature. The spin state of Co^{3+} cations evolves from $S = 0$ (low-spin, LS) at low temperatures to $S = 1$ (intermediate-spin, IS) at intermediate temperatures and subsequently to $S = 2$ (high-spin, HS) at high temperatures. In RCoO$_3$ (R = rare-earth ions) the spin state transition is associated with thermal excitation and not with a phase transition [41–44]. This means an increase in spin states population with temperature that accounts for a wide change in the paramagnetic moment. A similar proposal concerning a change in population of states is presented in the work of Lubinskii *et al.*, published in 2008 [45]. In this work, magnetization studies on NdCo$_{1-x}$Ga$_x$O$_3$ are reported. They took two temperature ranges above the magnetic transition, 130–370 and 600–940 K. They proposed a percentage of occupancy of Co^{3+} spin states. In the first temperature range, depending on the x value, LS and IS states or IS and HS are populated; at the second range, they proposed that Co^{3+} ions were in HS state except for $x = 0$ where Co^{3+} ions were in IS state.

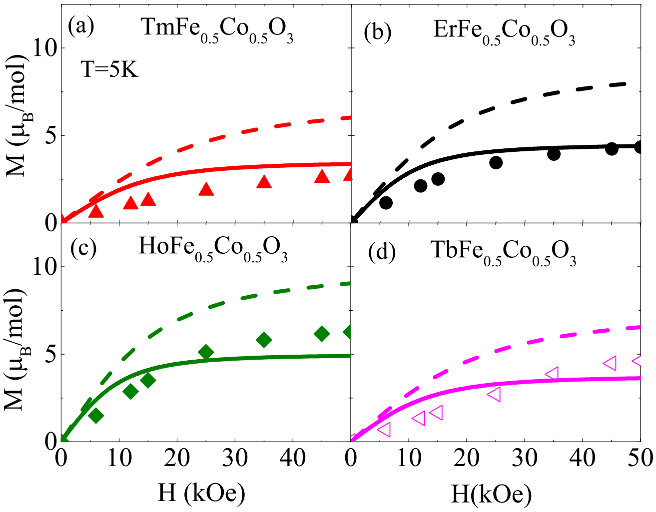

FIG. 5. [(a)–(d)] Magnetization (M) versus magnetic field (H) at temperature $T = 5$ K. Symbols are experimental data. Dashed lines indicate paramagnetic magnetization calculated from Brillouin expression for R^{3+} ions. Solid lines indicate magnetic calculation of an effective doublet $S = 1/2$ with $g_{\rm eff} = g_{\rm eff\parallel} = 2g.\,J$ and $g_{\rm eff\perp} = 0$, where g is the Landé factor for R^{3+} ion.

Isothermal magnetization curves at $T = 5$ K and up to $H = 50$ kOe are shown in Fig. 5. At this low temperature, the contribution of the AFM ordered Fe/Co lattice should be small and the dependence with H linear. In consequence, the experimental magnetization curves in Fig. 5 must be principally due to the magnetism of the R^{3+} magnetic moments and its paramagnetic behavior can be well modeled with the Brillouin expression:

$$M_B = Ng\mu_B J\left[\frac{\frac{2J+1}{2J}\coth\left(\frac{2J+1}{2J}y\right) - \frac{1}{2J}\coth y}{2J}\right]$$

$$M_B = Ng\mu_B J B_J(y)\,, \quad \text{where} \quad y = \frac{Jg\mu_B H}{kT}, \quad (3)$$

where B$_J$ is the Brillouin function, J is the quantum number associated with the total angular moment, and g is the Landé factor. Equation (3) has saturation at low temperatures or at high magnetic field values. The expected magnetization for the paramagnetic ions R^{3+} were simulated using the g and J values reported for fundamental states of this ions and the simulated curves are presented with dashed lines in Fig. 5. In all cases, the experimental data are lower than the magnetizations expected for free paramagnetic R^{3+} ions. The magnetization at $T = 5\,\mathrm{K}$ and $H = 50\,\mathrm{kOe}$ (M_s) and the expected values for free paramagnetic ions (M_B) are presented in Fig. 9(a). Although M_s is nearly a half of M_B, they have the same dependency with the rare-earth. This indicates that, despite the low values of magnetization, R^{3+} magnetic moment is the principal contribution to the magnetization.

In the work of A. Antunes *et al.*, reported in 2007 [46], it was shown that the magnetization of $\mathrm{ErCo}_{1\text{-}x}\mathrm{Mn}_x\mathrm{O}_3$ at low temperatures was dominated by the paramagnetic contribution of Er^{3+}, although it is not discussed in that work, the magnetic saturation value presented for $\mathrm{ErCo}_{0.4}\mathrm{Mn}_{0.6}\mathrm{O}_3$ [$M_s \approx 100\,\mathrm{emu/g}\,(4.8\,\mu_\mathrm{B})$], is lower than the expected for Er^{3+} $M_s = 9\,\mu_\mathrm{B}$. This behavior has been observed in other compounds like $\mathrm{R}_2\mathrm{Ti}_2\mathrm{O}_7$ pyrochlores [47]. In these oxides, the titanium ion is in 4+ oxidation state, it is diamagnetic, hence the only contribution to the magnetization is coming from the magnetic moment of R^{3+} ions. However, crystal-field effect breaks the degeneration of the fundamental state. The new levels structure explains the reduction of the magnetization values. Now, let us focalize on the Er^{3+} case, the fundamental state of which is a doublet ($S = 1/2$) under the crystal-field effects.

The thermally averaged magnetization of the two state model can be calculated making a powder averaging and assuming a doublet as fundamental state and considering the g factor parallel and perpendicular ($g_\parallel = g_\mathrm{eff}$ and $g_\perp = 0$) to the field direction respectively. Then, the expression that describes the model magnetization is

$$\frac{\langle\mu\rangle}{\mu_\mathrm{B}} = \frac{(kT)^2}{g_\mathrm{eff}\;\mu_\mathrm{B}{}^2H^2S}\int_0^{g_\mathrm{eff}\;HS/kT} x\tanh(x)\,dx \qquad (4)$$

Which can be numerically integrated [48]. In Fig. 5(b), the solid line represents the numerical integrated solution for $g_\mathrm{eff} = 2gJ$ at $T = 5\,\mathrm{K}$. The magnetization value obtained with this model is closer to the experimental data and the curve is a good approach. This is a simplified model that does not take into account the interactions at other levels. The same simulations were done for the other compounds and are presented in Fig. 5. The comparison between experimental data with Brillouin function and those simulated from crystal-field consideration allows us to conclude that at low temperatures the principal contribution to the R^{3+} magnetization is influenced by crystal-field effects. The deviation from the calculated curves and the experimental data can be due to interactions between Fe/Co and R or by the contribution of the magnetically ordered Fe/Co sublattice, both have not been considered in the calculations.

C. Electrical properties

Electrical conductivity (σ) for $R\mathrm{Fe}_{0.5}\mathrm{Co}_{0.5}\mathrm{O}_3$ compounds increases with temperature (T), which is usual in insulating materials. Different conductivity models were tested to fit the experimental data. A typical Arrhenius-like law [σ α exp $(-\frac{E_a}{kT})$, where E_a is the activation energy and k the Boltzmann constant] does not describe the obtained results. It is easily visualized when $\ln\sigma$ versus T^{-1} is plotted, that these curves do not have a clear linear dependence. In contrast, the σ α exp $(-\frac{E_a}{kT})$ behavior in the electrical conductivity was observed in orthoferrites ($R\mathrm{FeO}_3$) [49] where all iron ions are occupying the B site and there is no disorder in this crystallographic site.

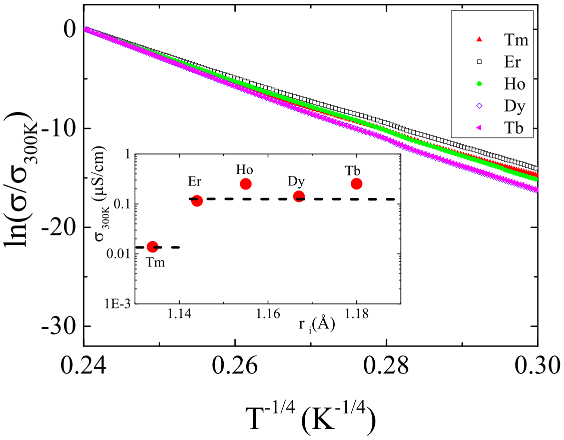

FIG. 6. Electrical conductivity ($\ln\sigma/\sigma_{300\,\mathrm{K}}$) for $R\mathrm{Fe}_{0.5}\mathrm{Co}_{0.5}\mathrm{O}_3$ with $R = \mathrm{Tm}$, Er, Ho, Dy, and Tb as a function of temperature ($T^{-1/4}$). The linear behavior of the experimental data indicates that the electric conduction mechanism is VRH (variable-range-hopping) type. (Inset) Electrical conductivity values at room temperature ($\sigma_{300\,\mathrm{K}}$), note the difference between Tm and the rest of the samples.

In particular, in systems with structural disorder, the most feasible mechanism to describe the electrical conductivity is the Mott's variable range hopping (VRH) model, where the hopping of carriers between the nearest next neighbor ions is proposed and whose temperature dependence is $\sigma = \sigma_0\exp(T_0/T)^{-1/4}$. Probably, in this case, the random occupancy of Fe/Co ions in the perovskite B site can be the source of disorder that defines the conduction mechanism. The linear behavior in a $\ln(\sigma/\sigma_{300\,\mathrm{K}})$ α $T^{-1/4}$ plot demonstrates the agreement between the experimental data and the VRH model, which is appreciable in Fig. 6. In the inset of this figure the room temperature dc conductivities are displayed. The values are between $0.15\,\mu\mathrm{S/cm} < \sigma < 0.25\,\mu\mathrm{S/cm}$ for $R = \mathrm{Er}$, Ho, Dy and Tb compounds, but the conductivity decreases ten times for $R = \mathrm{Tm}$, $\sigma \sim 0.015$ $\mu\mathrm{S/cm}$, being the most insulating compound of the series.

Figure 7 illustrates the real (a) and imaginary (b) component of the electrical permittivity ($\varepsilon^* = \varepsilon' - i\varepsilon''$) measured at 1 kHz. The low temperature ε' values are similar for Tm, Er, Ho, $16 < \varepsilon' < 20$, which are lower than the values for Dy and Tb, being $\varepsilon' = 25$ and $\varepsilon' = 39$ respectively. When T is increased, a shoulder in the ε' curve is observed only for $\mathrm{TmFe}_{0.5}\mathrm{Co}_{0.5}\mathrm{O}_3$. Indeed, the imaginary component ε'' [see Fig. 7(b)], which is associated with the electric loss, shows for $\mathrm{TmFe}_{0.5}\mathrm{Co}_{0.5}\mathrm{O}_3$ a completely different behavior in comparison with the other members of the series. In general, poor electrical conductivity is associated with low values of electric loss. At high temperatures, the ε'' values are one order

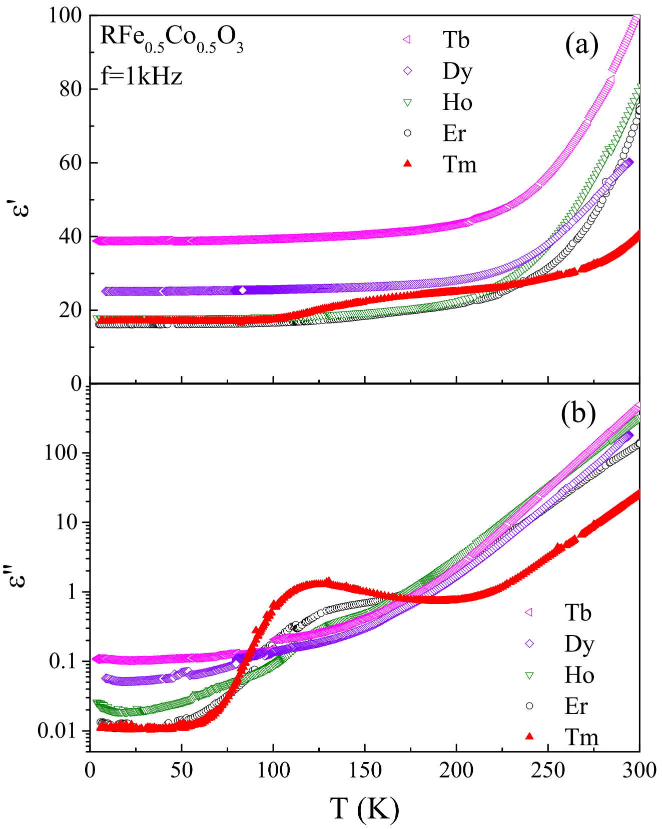

FIG. 7. (a) Real (ε') and (b) imaginary parts (ε'') of the electrical permittivity ($\varepsilon^* = \varepsilon' - i\,\varepsilon''$). Note in both plots, the significantly different behavior of Tm compound with respect the rest of the series. At room temperature, Tm sample presents values of ε'' one order of magnitude lower than the rest of the samples with larger ionic radii.

of magnitude lower in Tm sample than in the rest of the series, which is in agreement with the electrical conductivity values observed at room temperature (inset Fig. 6).

In order to study the multiferroic properties of all the analyzed perovskites, pyroelectric current measurements were carried out on these insulating samples, trying to detect remanent polarization on the samples. Polarizations versus temperature curves are obtained by integrating the data of the pyroelectric current measurements, which is obtained increasing the temperature. Previously, to induce a polarization (P), the samples were cooled under an electric field (E). These measurements are very hard to perform because of both, the low currents measured and the presence of other sources of currents like thermoelectric potential. In order to discard these spurious effects, a second run where the samples were cooled applying an electric field with the opposite sign ($-E$) to induce $-P$ was necessary. After this, the pyroelectric current was measured increasing the temperature in the same conditions that the first run, obtaining negative and symmetric values of current. Near room temperature, spurious currents were detected and subtracted, probably due to the presence of thermoelectric potential. We only detected pyroelectric currents (or polarization) in the most insulating $TmFe_{0.5}Co_{0.5}O_3$ sample.

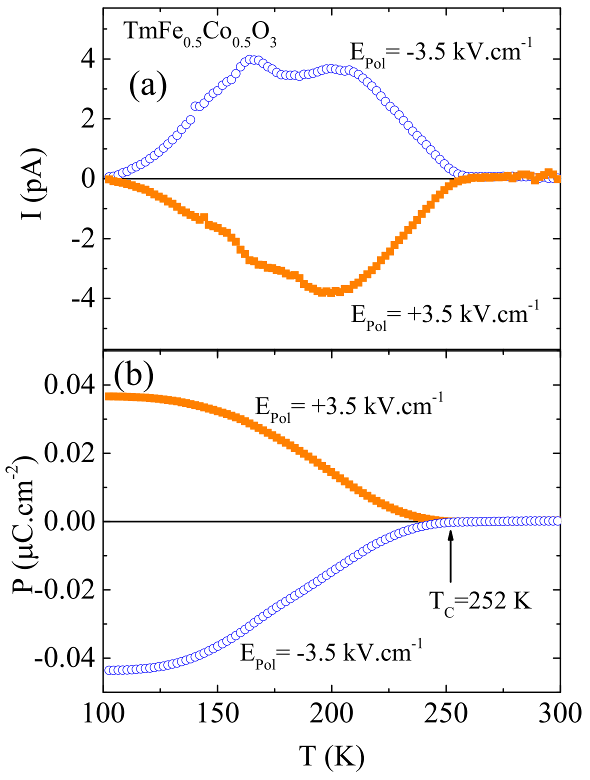

FIG. 8. (Top) Pyroelectric current measured increasing the temperature after cooling under an applied field ± 3.5 kV/cm. (Bottom) Electrical polarization (P) calculated by integrating I values as a function of T.

Figure 8 illustrates the pyroelectric current and polarization data for $TmFe_{0.5}Co_{0.5}O_3$. The polarization inverts its sign with the inversion of the applied electric field. Both polarization branches disappear at $T_C = 252\,\mathrm{K}$ (ferroelectric transition temperature). The polarization values $P = 0.035\,\mu\mathrm{C\,cm^{-2}}$ after cooling with $E = 3.5\,\mathrm{kV\,cm^{-1}}$ is higher than that observed in a single-crystal sample of $SmFeO_3$ ($P = 80\,\mu\mathrm{C/m^2}$) [11]. Besides, the ferroelectric transition temperature is really close to the weak ferromagnetic transition temperature. If we observe in detail ZFC and FC curves for $TmFe_{0.5}Co_{0.5}O_3$ [Fig. 2(a)], the weak ferromagnetic transition is wide and an increase of magnetization occurs between 220 and 250 K. This indicates that the ferroelectric order is associated with the magnetic order like in $SmFeO_3$ [11].

The dependence of the magnetization at 5 K as a function of ionic radii is presented in Fig. 9(a). The calculated values for R^{3+} free ions (M_B) are presented in solid line in this figure. Solid circles represent the experimental M_s data at 5 K, the same dependence is observed in both curves, but lower experimental values of M_s are observed, which we associated with crystal-field effect (see Fig. 5). The phase diagram presented in Fig. 9(b) shows the magnetic representation obtained from the refinement of NPD data, coherent with the magnetic transition temperatures (T_{N1} and T_SR) observed in the magnetic measurements (Figs. 2 and 3). We also represent in the diagram the FE behavior of $TmFe_{0.5}Co_{0.5}O_3$ below T_{N1}.

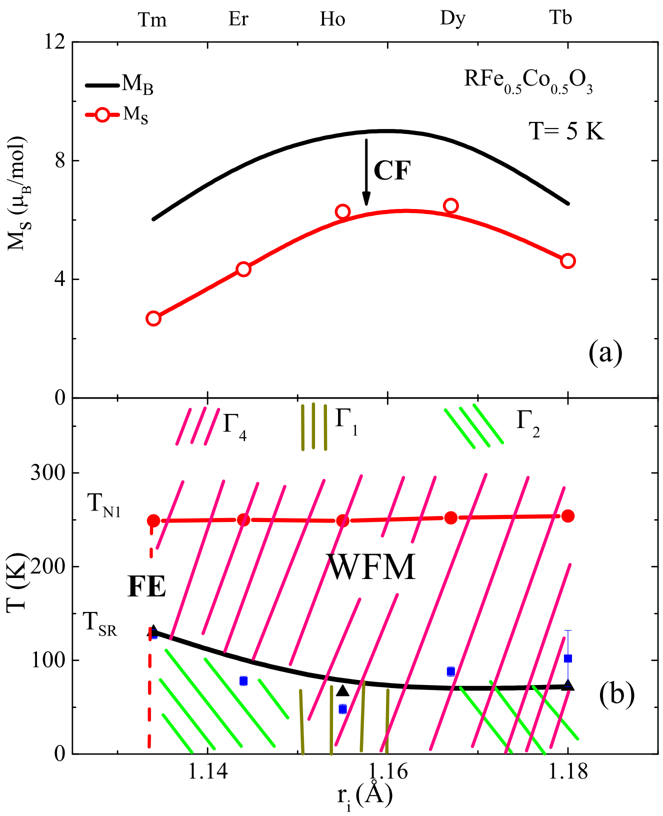

FIG. 9. (Top) (a) Saturation magnetization for $R\text{Fe}_{0.5}\text{Co}_{0.5}\text{O}_3$ with R = Tm, Er, Ho, Dy, and Tb. The experimental values (M_s) are lower (filled circles with solid line) than the expected (solid line) saturation of rare-earth magnetic moments (M_B). This effect is due to the crystal-field (CF) interaction. (Bottom) (b) Magnetic and electric phase diagram describing the transition metal (Fe/Co) sublattice behavior. Weak ferromagnetic order (WFM) is observed below room temperature. The characteristic temperature (T_{N1}) associated with the onset of magnetic order of the Fe/Co sublattice is represented by (•) in the plot. SR transitions are observed in the NPD data (▲) and the temperatures, at the maximum of M vs T in the ZFC curve, are represented by (■). $\text{TmFe}_{0.5}\text{Co}_{0.5}\text{O}_3$ has ferroelectric (FE) polarization at $T < 252$ K.

IV. CONCLUSIONS

A systematic study of the crystal and magnetic structure of the $R\text{Fe}_{0.5}\text{Co}_{0.5}\text{O}_3$ perovskites with R = Tm, Er, Ho, Dy, and Tb was performed by NPD measurements. Besides, its magnetic, electric and ferroelectric properties were exhaustively characterized by means of magnetization, electrical conductivity, dielectric permittivity and pyroelectric current measurements. All the compounds belong to the orthorhombic *Pbnm* space group. In the samples with R = Tm, Ho and Tb a NTE of a lattice parameter was observed, which is a clear evidence of magnetostrictive effects.

The refinements of NPD patterns at 2 K, 300 K, and intermediate temperatures show the reflections of the magnetically ordered transition metal sublattice (Fe/Co). In all the samples at temperatures close to 300 K, a Γ_4 irreducible representation describes the magnetic structure with the magnetic moments aligned, principally, along the x axis in a *G*-AFM/WFM order. On the other hand, with the exception of the Ho perovskite that at 2 K shows Γ_1 (*G*-AFM) irreducible representation, the remaining members of the series exhibit Γ_4 and Γ_2 irreducible representations that describe the magnetic structures. In these cases, also in a *G*-AFM/WFM order, the magnetic moments are aligned along the z axis. The G magnetic type order and their small FM component, which rotates from z to x axis, indicate weak ferromagnetic or canted antiferromagnetic order in the Fe/Co magnetic sublattice. Magnetization data under FC and ZFC protocols show different characteristics for each compound. The change of the slope in the magnetization curves close to $T_{N1} \sim 250\,\text{K}$ is considered to be the onset of magnetic order, although some correlations survive above T_{N1}. At lower temperatures, a maximum in the FC/ZFC curves is observed, which can be directly associated with the SR.

The analysis of the inverse of the magnetic susceptibility at high temperatures ($T > 700$ K) shows antiferromagnetic correlations and an experimental effective magnetic moment close to the expected sum of high-spin states of Co^{3+}, Fe^{3+}, and the corresponding R^{3+} paramagnetic moments. The deviation from the Curie-Weiss law at intermediate temperatures (300–650 K) can be explained by the change of the population of spin state configuration of the cobalt ions (from intermediate to high-spin) and also can contribute to this deviation some iron-iron ions correlations that survive above T_{N1}.

At low temperatures, magnetization values of the rare earth with H was described, and the reduced values observed were ascribed to the presence of single ion anisotropy of the crystal-field effects on R^{3+} ions.

The electrical conductivity of the samples can be described with a $T^{-1/4}$ temperature dependence behavior indicating the presence of Mott's variable-range-hopping mechanism, associated with the random occupation of Fe and Co in the B site of the perovskite. Direct current conductivity at 300 K for the Tm sample is ten times lower than for the other rare-earth compounds. In the Tm case the complex electrical permittivity shows different behavior than the other members of the series and the imaginary electric permittivity presents extra shoulders below 250 K. Finally, the Tm sample can be polarized when the sample is cooled under different values of electrical field (E). Pyroelectric current can be detected while the sample is warming and depolarized showing the ferroelectric critical temperature (T_C) very close to T_{N1} (observed in the magnetic data). A low electric polarization of 400 $\mu\text{C/m}^2$ was measured for $\text{Tm}\,\text{Fe}_{0.5}\text{Co}_{0.5}\text{O}_3$. No electric polarization was detected in the rest of the studied members.

ACKNOWLEDGMENTS

R.D.S. acknowledges support from the Agencia Nacional de Promoción Científica y Tecnológica (ANPCyT), PICT-2017-0725 and the Secretaría de Ciencia, Tecnología y Posgrado de la Universidad Nacional de Cuyo, (SECTyP-UNCuyo), Project 06/C519. R.E.C. thanks support from Consejo Nacional de Investigaciones Científicas y Técnicas (CONICET), PIP No. 11220120100360, the Agencia Nacional de Promoción Científica y Tecnológica (ANPCyT), PICT-2016-2495 and the Secretaría de Ciencia y Tecnología de la Universidad Nacional de Córdoba (SECyT-UNC), Project 113/17. Project 203/14. J.A.A. thanks the Spanish Ministry of Economy and Competitivity through Grant MAT2017-84496-R. We gratefully acknowledge Paul Scherrer Institute PSI (Villigen, Switzerland) for access to neutron powder diffractometers. The work was partially performed at the Swiss Spallation Neutron Source SINQ (PSI). F. P. and J. L. thank CONICET for a fellowship.

J.L. and F.P. contributed equally to this work.

---

[1] T. Kimura, G. Lawes, T. Goto, Y. Tokura, and A. P. Ramirez, Phys. Rev. B **71**, 224425 (2005).

[2] S. W. Cheong and M. Mostovoy, Nat. Mater. **6**, 13 (2007).

[3] R. Ramesh and N. A. Spaldin, Nat. Mater. **6**, 21 (2007).

[4] V. Laukhin, V. Skumryev, X. Martí, D. Hrabovsky, F. Sánchez, M. V. García-Cuenca, C. Ferrater, M. Varela, U. Lüders, J. F. Bobo, and J. Fontcuberta, Phys. Rev. Lett. **97**, 227201 (2006).

[5] Y. Tokura, and S. Seki, Adv. Mater. **22**, 1554 (2010).

[6] N. Spaldin, MRS Bulletin **42**, 385 (2017).

[7] Y. Tokura, S. Seki, and N. Nagaosa, Rep. Prog. Phys. **77**, 076501 (2014).

[8] R. L. White, J. Appl. Phys. **40**, 1061 (1969).

[9] D. Treves, J. Appl. Phys. **36**, 1033 (1965).

[10] U. Chowdhury, S. Goswami, D. Bhattacharya, J. Ghosh, S. Basu, and S. Neogi, Appl. Phys. Lett. **105**, 052911 (2014).

[11] J. H. Lee, Y. K. Jeong, J. H. Park, M. A. Oak, H. M. Jang, J. Y. Son, and J. F. Scott, Phys. Rev. Lett. **107**, 117201 (2011).

[12] S. Acharya, J. Mondal, S. Ghosh, S. Roy, and P. Chakrabarti, Mat. Lett. **64**, 415 (2010).

[13] M. Shang, C. Zhang, T. Zhang, L. Yuan, L. Ge, H. Yuan, and S. Feng, App. Phys. Lett. **102**, 062903 (2013).

[14] J. B. Goodenough and J. M. Longo, *Landolt Börnstein*, New Series III (Springer, New York, 1970), Vol. 4a.

[15] P. Ganguly and C. N. R. Rao, Bull. Mater. Sci. **2**, 193 (1980).

[16] J. A. Alonso, M. J. Martínez-Lope, C. de la Calle, and V. Pomjakushin, J. Mater. Chem. **16**, 1555 (2006).

[17] P. M. Raccah and J. B. Goodenough, Phys. Rev. **155**, 932 (1967).

[18] P. Mandal, V. S. Bhadram, Y. Sundarayya, C. Narayana, and A. Sundaresan, C. N. R. Rao, Phys. Rev. Lett. **107**, 137202 (2011).

[19] B. Rajeswaran, P. Mandal, R. Saha, E. Suard, A. Sundaresan, and C. N. R. Rao, Chem. Mater. **24**, 3591 (2012).

[20] F. Pomiro, R. D. Sánchez, G. Cuello, A. Maignan, C. Martin, and R. E. Carbonio, Phys. Rev. B **94**, 134402 (2016)

[21] Y. Nagata, S. Yashiro, T. Mitsuhashi, A. Koriyama, Y. Kawashima, and H. Samata, J. Mag. Mag. Mater. **237**, 250 (2001).

[22] M. Mihalik, M. Mihalik, M. Fitta, M. Bałanda, M. Vavra, S. Gabáni, M. Zentková, and J. Briancin, J. Mag. Mag. Mater. **345**, 125 (2013).

[23] E. Traversa, P. Nunziante, M. Sakamoto, Y. Sadaoka, and R. Montanari, Mater. Res. Bull. **33**, 673 (1998).

[24] D. M. Gil, J. Guimpel, A. Paesano, R. E. Carbonio, and M. I. Gómez, J. Mol. Struct. **1015**, 112 (2012).

[25] H. M. Rietveld, J. Appl. Crystallogr. **2**, 65 (1969).

[26] J. Rodríguez-Carvajal, Phys. B Condens. Matter **192**, 55 (1993).

[27] See Supplemental Material at http://link.aps.org/supplemental/10.1103/PhysRevB.98.134405 for a, b and c lattice parameters as a function of temperature for $R\mathrm{Fe}_{0.5}\mathrm{Co}_{0.5}\mathrm{O}_3$ with $R = \mathrm{Tm}$, Ho and Tb.

[28] J. C. Wood, Bull. Am. Phys. Soc. **13**, 574 (1968).

[29] J. Träff, Physica Stat. Sol. (b) **34**, K139 (1969).

[30] F. J. Berry, J. Gancedo, J. F. Marco, and X. Ren, J. Sol. State Chem. **177**, 2101 (2004).

[31] T. Yamaguchi, J. Phys. Chem. Solids **35**, 479 (1974).

[32] R. M. Hornreich, J. Mag. Mag. Mat. **7**, 280 (1978).

[33] X. Liu, L. Hao, Y. Liu, X. Ma, S. Meng, Y. Li, J. Gao, H. Guo, W. Han, K. Sun, M. Wu, X. Chen, L. Xie, F. Klose, and D. Chen, J. Mag. Mag. Mat. **417**, 382 (2016).

[34] A. V. Kimel, A. Kiriyuk, A. Tsvetkov, R. V. Pisarev, and Th. Rasing, Nature **429**, 850 (2004).

[35] G. Deng, P. Guo, W. Ren, S. Cao, H. E. Maynard-Casely, M. Avdeev, and G. J. McIntyre, J. Appl. Phys. **117**, 164105 (2015).

[36] T. Chatterji, M. Meven, and P. J. Brown, AIP Adv. **7**, 045106 (2017).

[37] Z. Y. Zhao, X. Zhao, H. D. Zhou, F. B. Zhang, Q. J. Li, C. Fan, X. F. Sun, and X. G. Li, Phys. Rev. B **89**, 224405 (2014).

[38] S. Artyukhin, M. Mostovoy, N. Jensen, D. Le, K. Prokes, V. G. de Paula, H. N. Bordallo, A Maljuk, S. Landsgesell, H. Ryll, B. Klemke, S. Paecke, K. Kiefer, K. Lefmann, L. T. Kuhn, and D. N. Argyriou, Nat. Mater. **11**, 694 (2012).

[39] E. F. Bertaut, Acta Crystallogr. Sect. A **24**, 217 (1968).

[40] A. Muñoz, M. J. Martínez-Lope, J. A. Alonso, and M. T. Fernández-Díaz, Eur. J. Inorg. Chem. **2012**, 5825 (2012).

[41] T. Kyômen, Y. Asaka, and M. Itoh, Phys. Rev. B **71**, 024418 (2005).

[42] M. Tachibana, T. Yoshida, H. Kawaji, T. Atake, and E. Takayama-Muromachi, Phys. Rev. B **77**, 094402 (2008).

[43] S. Yamaguchi, Y. Okimoto, and Y. Tokura, Phys. Rev. B **54**, R11022 (1996).

[44] C. Zobel, M. Kriener, D. Bruns, J. Baier, M. Grüninger, T. Lorenz, P. Reutler, and A. Revcolevschi, Phys. Rev. B **66**, 020402(R) (2002).

[45] N. N. Lubinskii, L. A. Bashkirov, A. I. Galyas, S. V. Shevchenko, G. S. Petrov, and I. M. Sirota, Inorg. Mater. **44**, 1015 (2008).

[46] A. Antunes, O. Peña, C. Moure, V. Gil, and G. André, J. Mag. Mag. Mat. **316**, e652 (2007).

[47] S. T. Bramwell, M. N. Field, M. J. Harris, and I. P. Parkin, J. Phys.: Cond. Matt. **12**, 483 (2000).

[48] R. J. Elliot and K. W. H. Stevens, Proc. Roy. Soc. A **218**, 553 (1953).

[49] G. V. Subba Rao, B. M. Wanklyn, C. N. R. Rao, J. Phys. Chem. Solids **32**, 345 (1971).